

pubs.acs.org/acscatalysis Research Article

Revised Nitrogen Reduction Scaling Relations from Potential-Dependent Modeling of Chemical and Electrochemical Steps

Cooper R. Tezak, Nicholas R. Singstock, Abdulaziz W. Alherz, Derek Vigil-Fowler, Christopher A. Sutton, Ravishankar Sundararaman, and Charles B. Musgrave*



Cite This: ACS Catal. 2023, 13, 12894-12903



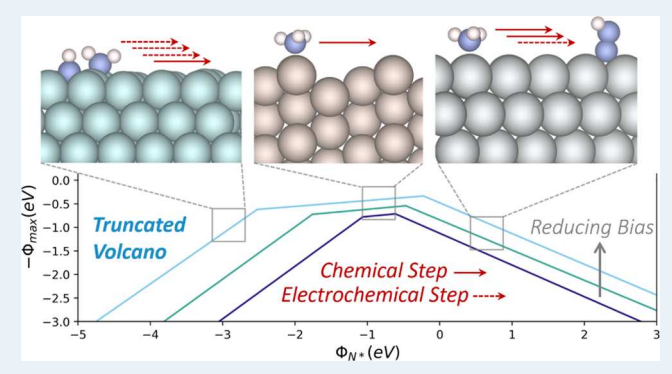
ACCESS I

Metrics & More

Article Recommendations

sı Supporting Information

ABSTRACT: The electrochemical nitrogen reduction reaction (NRR) is a promising route to enable carbon-free ammonia production. However, this reaction is limited by the poor activity and selectivity of current catalysts. The rational design of superior NRR electrocatalysts requires a detailed mechanistic understanding of current material limitations to inform how these might be overcome. The current understanding of how scaling limits NRR on metal catalysts is predicated on a simplified reaction pathway that considers only proton-coupled electron transfer (PCET) steps. Here, we apply grand-canonical density functional theory to investigate a more comprehensive NRR mechanism that includes both electrochemical and chemical steps on 30 metal surfaces in solvent under an applied potential. We applied $\Phi_{\rm max}$, a grand-



canonical adaptation of the $G_{\rm max}$ thermodynamic descriptor, to evaluate trends in catalyst activity. This approach produces a $\Phi_{\rm max}$ "volcano" diagram for NRR activity scaling on metals that qualitatively differs from the scaling relations identified when only PCET steps are considered. NH₃* desorption was found to limit the NRR activity for materials at the top of the volcano and truncate the volcano's peak at increasingly reducing potentials. These revised scaling relations may inform the rational design of superior NRR electrocatalysts. This approach is transferable to study other materials and reaction chemistries where both electrochemical and chemical steps are modeled under an applied potential.

KEYWORDS: electrocatalysis, nitrogen reduction, grand-canonical DFT, scaling relations, energetic span

■ INTRODUCTION

The synthesis of ammonia as a precursor to fertilizer is estimated to support the nutritional needs of more than 40% of the world's population.^{1,2} Furthermore, ammonia is a promising carbon-free fuel and hydrogen carrier for applications in sustainable transportation and energy storage. Ammonia is most commonly synthesized by the Haber-Bosch process, using hydrogen produced from methane reforming and energy generated from hydrocarbon combustion, and accounts for nearly 2% of global carbon emissions. There are two primary approaches to decarbonize ammonia synthesis: the "Green" Haber-Bosch process using hydrogen produced via water electrolysis³ or solar thermochemical water splitting,⁴ and the electrochemical nitrogen reduction reaction (NRR).5 NRR provides the advantages of distributed, loadmatching production to generate ammonia near its point of use and can provide lower capital and operating expenses than the "Green" Haber-Bosch process. 5,6 However, current electrocatalysts for NRR are limited by poor selectivities and/or low activities that make commercialization infeasible. Efforts to improve the performance of NRR electrocatalysts are therefore

essential for the development of a sustainable ammonia synthesis process.

Over the past two decades, research efforts aimed at identifying superior NRR electrocatalysts have increased significantly.⁷ Computational mechanistic studies have also been conducted to gain a better understanding of the nitrogen reduction mechanism at the catalyst surface with the aim of guiding the discovery of new NRR electrocatalysts.^{8–12} Computational investigations of NRR catalyzed by metals predicted that NRR on metal surfaces obeys scaling relations between key reaction intermediates, resulting in a classic "volcano plot" for NRR activity, following the Sabatier principle.^{8,9} In particular, the scaling of the adsorption energy of the N₂H* state with the adsorption energy of the NH₂* state (where * indicates an adsorbed species) was predicted to

Received: May 2, 2023
Revised: August 3, 2023
Published: September 19, 2023





limit the minimum overpotential for NRR on metals, resulting in poor NRR activity at lower reducing potentials and intense competition with the hydrogen evolution reaction (HER) at higher reducing potentials.

The studies that identified the scaling relations that limit NRR activity have impacted the NRR field profoundly and continue to guide screening studies. 12-15 However, these studies did not consider the effects of solvation and approximated the fixed electrochemical potential of the electrocatalyst interface using the posthoc computational hydrogen electrode (CHE) method. Moreover, these studies only considered the proton-coupled electron transfer (PCET) steps of the NRR mechanism (Figure 1A) because the CHE

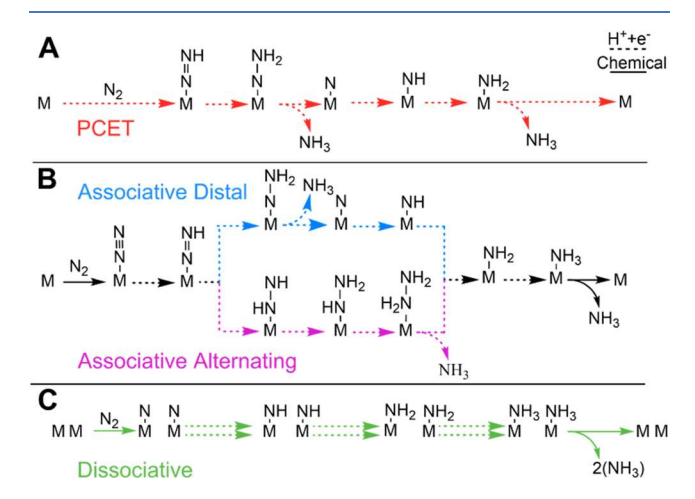


Figure 1. Pathways for NRR on an electrocatalyst surface. The pathways used to model NRR include: (A) PCET, (B) associative distal, associative alternating, and (C) dissociative. M represents the active site on the electrocatalyst surface. Chemical (i.e., non-PCET) steps are represented by solid reaction arrows, and electrochemical (i.e., PCET) steps are represented by dashed arrows. The double arrows in (C) indicate that two PCET steps take place for both dissociated intermediates.

method and conventional fixed-charge density functional theory (DFT) do not model the bias dependence of non-PCET steps. Thus, these studies neglect the possibility that non-PCET steps could be rate-limiting under specific electrochemical conditions. Recent studies of NRR on unconventional materials have included non-PCET reaction steps in their analysis and find that ignoring non-PCET steps (i.e., chemical steps) yields qualitatively different activity trends. 10,16,17 However, NRR scaling relations on metals have not yet been reexamined using a more complete mechanism that includes both electrochemical and chemical steps under applied bias. Consequently, there is a significant need to reevaluate NRR scaling on metals using a more comprehensive mechanism and methods that more accurately describe the effects of solvation and the applied potential to determine whether chemical steps play a significant role in directing NRR

Multiple NRR reaction pathways have been proposed, including the PCET pathway (Figure 1A) that was used to predict the prevailing NRR scaling relations for metals. However, because the PCET pathway excludes the chemical steps of N₂ adsorption and NH₃* desorption, it does not consider the possibility that these steps could be rate-limiting. In this work, we reevaluate NRR scaling on metals using a

more comprehensive mechanism that we call the "composite mechanism", which includes a range of proposed pathways, with both electrochemical and chemical steps. The composite mechanism includes: (1) the associative distal pathway (Figure 1B), (2) the associative alternating pathway (Figure 1B), and (3) the dissociative pathway (Figure 1C). The associative distal pathway is composed of similar intermediates as the PCET pathway but also includes N₂ adsorption and NH₃* desorption. The alternating pathway differs from the distal pathway in that the proximal nitrogen is protonated in an alternating sequence with protonation of the distal N. The dissociative pathway is initiated via dissociation of the N2 molecule, which is generally considered kinetically inaccessible due to the large barrier to break the N2 triple bond. However, recent work indicates that later dissociation of the nitrogen atoms may be kinetically accessible after associative adsorption and protonation to the NHNH* state, in which the N atoms are not bound through a triple bond.

In this work, Φ_{max} was calculated from grand-canonical density functional theory (GC-DFT) computed free energy diagrams for 30 metal surfaces and found to scale linearly with the N* adatom binding energy, resulting in Φ_{max} volcano plots. Our results predict that the chemical step of NH₃* desorption is a component of the energetic span for every surface considered here, and consequently that NH3* desorption limits the thermodynamics and likely the kinetics of NRR on metal surfaces. Because NH3* desorption is a chemical step, it is less sensitive to the applied potential than are PCET steps. Consequently, at more reducing potentials, it becomes more limiting and truncates the Φ_{max} volcano plot. Furthermore, we demonstrate that Φ_{max} shifts nonlinearly with bias on surfaces where the energetic span changes with bias. These results indicate the need to include both electrochemical and chemical steps when modeling the NRR on electrocatalyst surfaces. This requires an approach, such as GC-DFT, that captures the potential dependence of chemical steps. The modeling and analysis approach developed here that combines GC-DFT and $\Phi_{
m max}$ can be readily applied to other electrochemical reactions and material classes. Furthermore, because this approach is computationally efficient relative to a full kinetic evaluation, that is, computing transition states for each step under an applied bias, it can be applied to high-throughput studies to enable the generation of an electrocatalyst database. The database could be used for the broad investigation of materials and reactions to accelerate the understanding of electrochemical mechanisms and the discovery of advanced materials for a range of important electrochemical conversions including NRR to synthesize ammonia.

METHODS

GC-DFT Modeling. To model the composite NRR mechanism with applied potential and solvation, we used GC-DFT to study 30 d-block metal surfaces at 0.0, -0.25, and -0.5 V vs the standard hydrogen electrode (SHE). GC-DFT self-consistently solves the Kohn-Sham DFT equations for a system under a fixed applied potential (i.e., voltage or Fermi level) and allows the number of electrons to equilibrate self-consistently with the external potential. Surface charge is balanced by varying the ion number in an implicit electrolyte solvation model. Thus, GC-DFT treats the system as thermodynamically open with respect to the exchange of electrons and electrolyte ions with the external electron and ion reservoirs and computes grand free energies, represented in

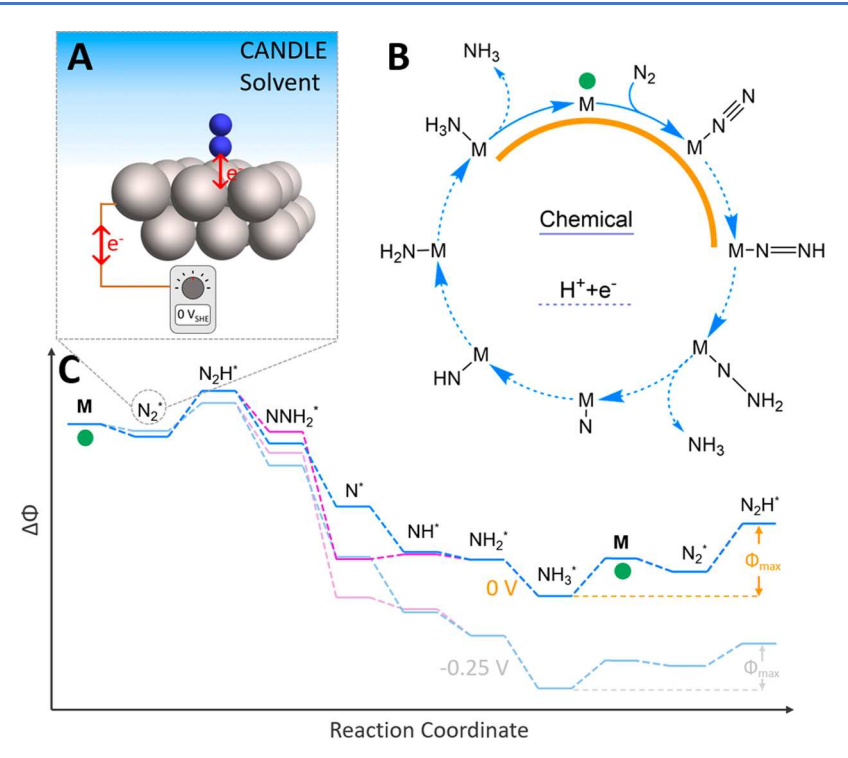


Figure 2. Graphical representation of Φ_{max} modeling approach. (A) Representation of a Ru(111) surface with an adsorbed N_2^* molecule modeled under solvation and applied bias. (B) Catalytic cycle for the associative distal pathway of the composite mechanism. (C) Grand free energy diagram of this catalytic cycle on Ru(111) at 0 V vs SHE. Magenta lines correspond to the associative alternating pathway, and blue lines correspond to the associative distal pathway. The orange curve in (B) indicates the energetic span steps, and the corresponding Φ_{max} value is shown in (C). The lighter lines in (C) are the free energy diagrams at -0.25 V.

this work as Φ . This enables a more realistic description of the electrified interface between the electrocatalyst surface and the electrolyte at electrochemical potentials set by the external potential (Figure 2A). Moreover, GC-DFT enables the non-PCET steps of the composite mechanism to be modeled as a function of the applied potential in contrast to neglecting them or assuming that their energetics have no potential dependence. Consequently, chemical (i.e., non-PCET) steps may still be associated with the transfer of electron density, resulting in bias dependence of these steps. Similarly, electrochemical (i.e., PCET) steps may be accompanied by noninteger electron transfers, resulting in a bias dependence of these steps that deviates from that estimated by CHE, which assumes one electron is transferred per PCET step. Furthermore, GC-DFT has predicted changes in the binding geometries of adsorbed species with changes in applied potential that would not be captured using conventional constant charge DFT. 16,20

$$\Phi_{\text{max}} = \begin{cases}
I_k^{\text{max}} - I_j^{\text{min}} & \text{if} \quad k \ge j \\
I_k^{\text{max}} - I_j^{\text{min}} - \Delta \Phi_{rxn} & \text{if} \quad k \le j
\end{cases}$$
(1)

where I_k^{max} and I_i^{min} are grand free energies of states k and j on a reaction pathway on which they are the highest- and lowestlying states, respectively, and so maximize Φ_{max} . A $\Delta\Phi$ can be calculated between any two states along the reaction pathway (i.e., any energetic span); however, only states k and j will maximize $\Delta\Phi$ to yield Φ_{max} . $\Delta\Phi_{rxn}$ is the free energy of the reaction. If the highest-lying intermediate, I^{max}, comes after the lowest-lying intermediate, I^{\min} (i.e., $k \ge j$), then Φ_{\max} is simply the difference in the free energy of the intermediates. However, if the order of the intermediates is reversed, and I^{max} comes before I^{\min} (i.e., k < j), the reaction free energy must be subtracted from the difference in intermediate energies due to the cyclic nature of the catalytic cycle (see SI Section 1.2 for more details). Consequently, Φ_{max} will be the same regardless of which states are selected for the beginning and end of the catalytic cycle. Figure 2C shows an energetic span in which the highest state comes before the lowest state and shows that the calculated energetic span must extend across the start of the cycle (indicated by the green circle), which is achieved by subtracting the reaction energy from the difference in energy of the highest and lowest states. The free energy change of the energetic span is conceptualized as an approximation to the activation energy of a catalytic cycle, and under the quasiequilibrium approximation, can be related to catalyst activity. 26,27

 $\Phi_{\rm max}$ serves as a general catalytic activity screening descriptor that applies to both PCET and non-PCET steps and can be calculated at any applied potential. Figure 2B shows

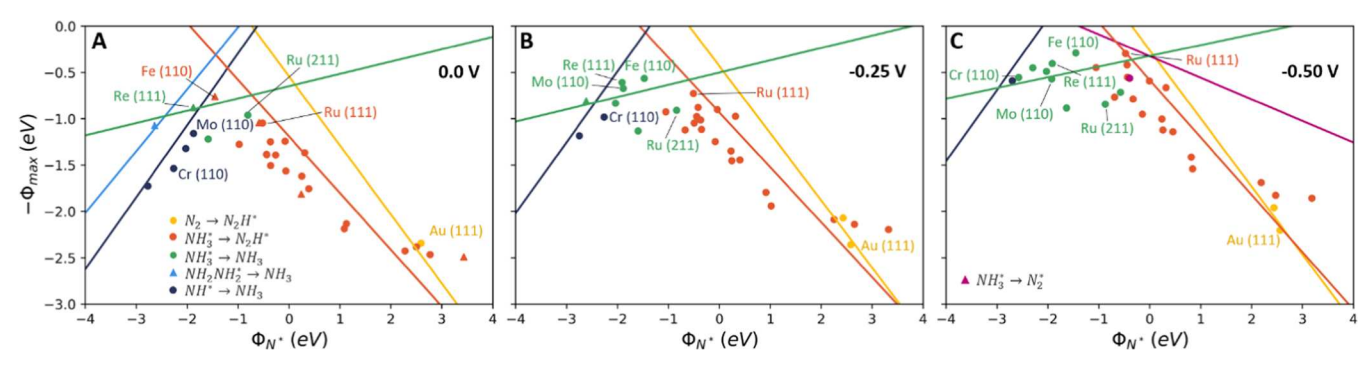


Figure 3. Φ_{max} scaling analysis for metal surfaces. $-\Phi_{max}$ plotted as a function of N* binding energy (Φ_{N^*}) at (A) 0 V, (B) -0.25 V, and (C) -0.5 V vs SHE. The colors of the lines correspond to the energetic span from which Φ_{max} is calculated, as shown in the legends. Triangles indicate materials where Φ_{max} is limited by an energetic span from the associative alternating pathway, whereas circles indicate energetic spans from the associative distal pathway or energetic spans shared between these two pathways. In (C), the magenta line appears because a new energetic span emerges at -0.5 V that did not appear for less reducing biases. The volcano diagrams become progressively more truncated by *NH₃ desorption as the bias is made more reducing.

a representative associative distal catalytic cycle for NRR on Ru(111), where a clean active site (green circle in Figure 2B) cyclically proceeds through N2 adsorption, six protonation steps, and finally, NH3* desorption to regenerate the clean active site. The reaction free energy diagram in Figure 2C shows that Φ_{max} , displayed in orange, is the largest endergonic change in free energy for the reaction free energy diagram. The states that define Φ_{max} (NH₃* and N₂H* in Figure 2C) also define the energetic span, which is displayed in the same color to span the same reaction intermediates in the cycle shown in Figure 2B. Φ_{max} was calculated for the associative distal, associative alternating, and dissociative pathways, but only the most exergonic Φ_{max} was used to analyze the reaction network. More reaction flux will flow through the pathway with the lower effective kinetic barrier, ^{28,29} and thus the most exergonic Φ_{max} in the reaction network was used to predict the activity of a material.

GC-DFT Calculation Details. Thirty d-block metal surfaces were modeled with GC-DFT using JDFTx. 18 Similar constant-potential DFT implementations have also previously been applied to model electrochemical reaction pathways. 30-32 The CANDLE implicit solvent model¹⁹ was used to account for the effects of the aqueous electrolyte at the electrochemical interface. All bulk crystal structures were taken from the Materials Project.³³ All bulk lattice constants were first optimized in JDFTx, from which surface facets were obtained using Pymatgen.³⁴ Following the approach of Montoya,⁸ the (110) surface facets were cut from body-centered cubic bulk structures and the (111) and (211) surfaces were cut from face-centered cubic structures. We note that the minimum energy crystal structure for Ru and Co is hexagonal closepacked, but cubic structures were used here to reproduce the approach of Montoya,8 and deconvolute the effects of bulk crystal phase. Ru(0001) cut from the hexagonal close-packed crystal structure was also modeled to determine the effect of the bulk crystal structure on activity prediction. The top and bottom faces of each slab are separated by 20 Å of space to provide a sufficient distance for charge screening by the solvation model. The flat (110), (0001), and (111) surfaces have $3 \times 3 \times 3$ atoms per unit cell. The stepped (211) surfaces have $3 \times 3 \times 4$ atoms per unit cell. The bottom layer of surface atoms was frozen to a bulk geometry. Surfaces (with and without adsorbates) are converged to 0.1 meV (0.0001 eV) by relaxing the ionic positions. All of the converged structures in

this work can be found at https://github.com/cote3804/NRR_data, which also includes the standardized calculation parameter files. All surfaces and their corresponding reaction energy diagrams are provided in Supporting Information.

JDFTx optimization was implemented in the Atomic Simulation Environment (ASE).³⁵ All structure optimization scripts used here are available at https://github.com/Nick-Singstock/GCNEB. 16 The GGA PBE functional 36 with D3 dispersion corrections³⁷ were used for all calculations together with an energy cutoff of 20 hartree (544 eV) and a charge density cutoff of 100 hartree. All calculations were converged with spin polarization and initialized with a magnetic moment of zero, with the exception of Co and Fe, which were initialized in a high-spin state to obtain consistent magnetic ordering. The Coulomb interaction was truncated in the z-direction for surface calculations to prevent self-interaction. Aqueous electrolyte was modeled using H2O as the solvent with ion concentrations of 0.5 M for F- and Na+ ions. The absolute potential of 4.66 eV for the standard hydrogen electrode was previously calibrated for the CANDLE solvent model by fitting experimental work functions to calculated chemical potentials.38

To model the composite mechanism on each surface, 11 NRR intermediates were studied: N_2^* , N_2H^* , NNH_2^* , NNH_3^* , N^* , NH^* , $NHNH^*$, $NHNH_2^*$, $NH_2M_2^*$, NH_2^* , and NH_3^* . Three additional adsorbates were also studied for three of the surfaces (see SI Section 2.6): *NNH $_3$, *NHNH $_3$, *NH $_2$ NH $_3$. Adsorbates were bound to each surface in three different binding configurations: atop, bridge, and 3 atom hollow sites. The lowest energy binding configuration for each intermediate was taken as the ground state and used in the $\Phi_{\rm max}$ analysis. A hydrogen adatom was also bound at the atop sites for each surface to model HER. Each clean surface and set of adsorbed structures were modeled at three biases: 0, -0.25, and -0.5 V vs SHE. In total, more than 3500 surface and adsorbate optimizations were performed.

The change in the grand free energy, $\Delta\Phi$, is the appropriate free energy term for the grand-canonical ensemble, which is open to the exchange of electrons with a reservoir at a fixed chemical potential.

$$\Delta \Phi = \Delta E - \mu \Delta N - T \Delta S \tag{2}$$

where ΔE is the change in computed electronic energy, μ is the electron chemical potential set by the applied bias, ΔN is the

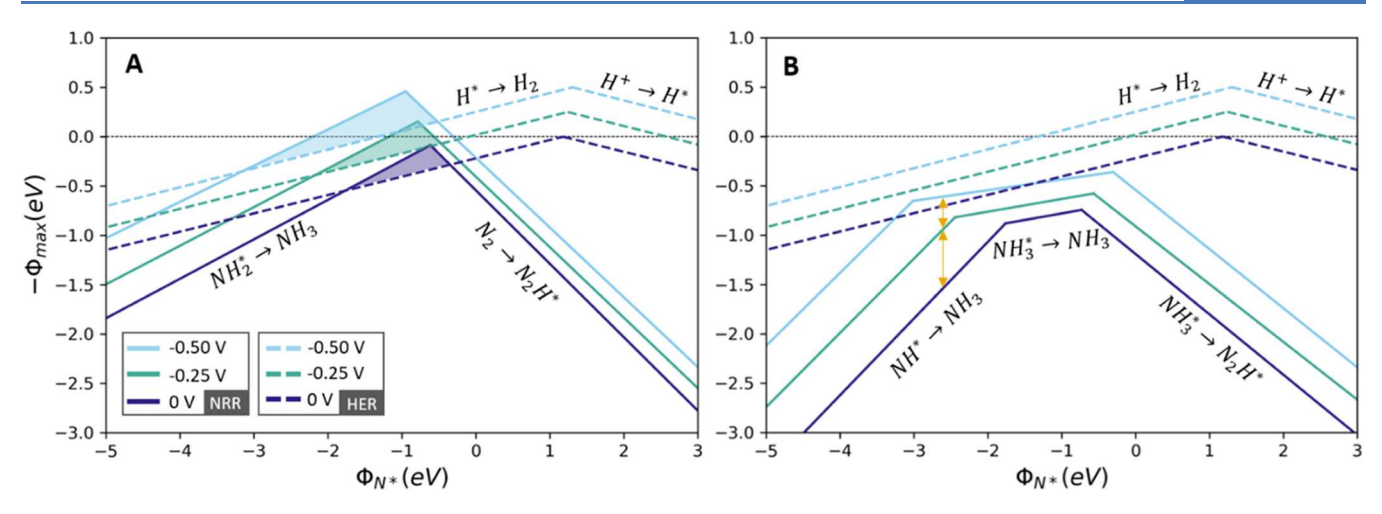


Figure 4. Comparison of the Φ_{max} screening descriptor or the PCET pathway and composite mechanism. (A) $-\Phi_{max}$ vs N* binding energy (Φ_{N^*}) at each bias using the PCET pathway. NRR scaling is represented by solid lines, and HER scaling by dashed lines. The steps that comprise the energetic spans are displayed next to the scaling lines. (B) $-\Phi_{max}$ vs Φ_{N^*} at each applied bias for the composite mechanism. Orange arrows show the nonlinear change in Φ_{max} for materials that switch from the NHNH₂* \rightarrow NH₃ line to the NH₃* \rightarrow NH₃ line at more reducing applied potentials.

change in the number of electrons, T is the temperature (298 K here), and ΔS is the change in entropy. Note that ΔN can be a noninteger. All degrees of freedom for adsorbed molecules were considered to be vibrational, similar to previous studies. The change in entropy for adsorption/desorption processes was calculated using gas phase molecular references from NIST. The change in vibrational entropy upon adsorption/desorption was 0.10 eV on Ru(111), which is below the significance threshold for $G_{\rm max}$ recommended by Exner. Because of the small change in vibrational entropy, the change in entropy is modeled in this work as the complete loss of translational and rotational entropy for adsorption/desorption processes only, which is on the order of 0.5 eV and cannot be considered insignificant.

Some surfaces dissociated intermediate states favorably during optimization. To ensure that dissociated state energetics were not being influenced by self-interaction, a Cr(110) supercell was modeled with the dissociative adsorbates (see Figure S2) and the binding energy of NH* + NH₂* and NH₂* + NH₂* was confirmed to differ by less than 0.07 eV from the smaller supercell model.

■ RESULTS AND DISCUSSION

Our calculations predict linear scaling between the free energy of NRR intermediates, which is consistent with previous studies that identified linear scaling between intermediates and the binding energy of an N* adatom $(\Phi_{N^*})^{.8-10}$ Linear scaling of intermediates with Φ_{N^*} results in linear scaling of the sequence of steps that comprise the energetic span with Φ_{N^*} . Consequently, Φ_{max} scales linearly with Φ_{N^*} for each energetic span. Figure 3 shows scatter plots of $-\Phi_{max}$ values vs Φ_{N^*} for each surface. Note that $-\Phi_{max}$ is plotted to reproduce the conventional upright volcano plot orientation, where highactivity materials lie near the volcano peak. Linear scaling lines between $-\Phi_{max}$ and Φ_{N^*} for each unique energetic span are also shown. These lines show how the energetic spans scale linearly as a function of Φ_{N^*} on all metal surfaces, and how different energetic spans limit Φ_{max} in different regions of the volcano plot. Note that all 30 metal surfaces were used to fit each scaling line by using the $\Delta\Phi$ associated with each energetic span, enabling scaling lines to be fit to the full data

set even for energetic spans that are only associated with $\Phi_{\rm max}$ for a single surface (e.g., Au(111) in Figure 3A). Fitting the scaling lines to all surface facets reduces the R^2 value relative to fitting the scaling lines to a single facet. However, the scaling trends remain the same when fit to individual facets (see SI Section 2.5), and the multifacet scaling lines shown in Figures 3 and 4 are expected to better generalize to other surface facets.

Figure 3 shows volcano-like scaling diagrams for Φ_{max} with Φ_{N^*} at each bias. As Φ_{N^*} changes, the binding energies of the reaction intermediates also change. This change in intermediate binding energies results in either a conserved energetic span, where the steps that make up the energetic span stay the same but Φ_{max} changes, seen as moving along a scaling line, or the steps that make up the energetic span change along with $\Phi_{\rm max}$, seen as shifting to a different scaling line. Thus, as $\Phi_{\rm N^*}$ changes, materials can move along the scaling lines or switch to new ones, but they cannot move significantly above the lowest scaling line at any Φ_{N^*} . The lines that comprise the volcano therefore define a minimum Φ_{max} (i.e., maximum $-\Phi_{max}$) at each $\Phi_{N^*}\!,$ and thus a boundary that limits $\Phi_{\text{max}}\!,$ beyond which no studied surfaces exist due to the inherent scaling relations between NRR intermediates. Because intermediates scale imperfectly with each other, some points deviate slightly above or below the boundary defined by the volcano (see SI

In contrast to previous studies where scaling between the adsorption energies of the N_2H^* intermediate and the NH_2^* intermediate limits the minimum overpotential, 8,9,40 several unique energetic span steps comprise this volcano and limit $\Phi_{\rm max}$ within certain N^* adatom binding ranges. More reactive surfaces on the left side of the volcano are limited by the formation of solvated NH_3 from NH^* (associative distal, dark blue scaling line) or $NH_2NH_2^*$ (associative alternating, light blue scaling line) intermediates. This results from the overbinding of intermediate adsorbates associated with a more favorable N^* adatom binding energy. The metals on the right side of the volcano are less reactive and thus tend to underbind the N_2^* and N_2H^* intermediates and are consequently limited by the $NH_3^* \to N_2H^*$ energetic span

(orange scaling line) that proceeds through the bare surface state (see Figure 2B).

At 0 V (Figure 3A), the shape of the Φ_{max} volcano is similar to previously predicted NRR activity volcanos (i.e., overpotential vs N*) for NRR on metals. 8,9 However, a key difference is that at 0 V a third region of the volcano emerges near the peak for materials with optimal N* binding and minimal Φ_{max} . This region is limited by the chemical step of NH₃* desorption from the catalyst surface (green scaling line). This step involves no proton-coupled electron transfers and is thus minimally dependent on the applied potential in contrast to other Φ_{max} limiting energetic spans that are composed of PCET steps. Consequently, as the applied potential becomes more reducing (Figure 3B,C), the y-intercept of the green scaling line associated with NH3* desorption increases at a rate lower than that of the other scaling lines that involve a PCET step. From 0.0 to -0.5 V, the y-intercept shifts from -0.65 to -0.32 eV for the chemical NH₃* desorption step scaling line $(\Delta = 0.33 \text{ eV}, 0 \text{ PCET steps})$, whereas the NH* to NH₃ scaling line shifts from 0.49 to 1.62 eV ($\Delta = 1.13$ eV, 2 PCET steps) and the NH₃* to N₂H* scaling line shifts from -1.19 to -0.58 eV ($\Delta = 0.61 \text{ eV}$, 1 PCET step). Thus, as the PCET steps become more favorable at more reducing biases, a greater number of materials become limited by the non-PCET step of NH₃* desorption. At -0.5 V, the most reducing potential considered here, a broader range of N* adatom binding energies exists where NH₃* desorption limits Φ_{max} . This results in a truncation of the volcano's peak and the inability of any of the surfaces studied herein to reach $\Phi_{max} \leq 0$ eV where all reaction steps are favorable. This agrees with experimental investigations of low-index transition metals, which are reported to have NH₃ activities <10 μ g/h⁻¹-g-catalyst.⁴

The PCET pathway (Figure 1A) does not consider chemical steps in the catalytic cycle, specifically the adsorption of N_2 or the desorption of N_{H_3} *. To compare the composite mechanism to the PCET mechanism, $-\Phi_{max}$ for both mechanisms is plotted in Figure 4A,B for each studied bias. In the PCET mechanism, the limiting energetic span steps for all materials and facets at 0 V are the reductive desorption $(N_{H_2})^* \rightarrow N_{H_3} + N_3$ and reductive adsorption $(N_2)^* \rightarrow N_2$. These are the same scaling relations identified by previous studies to limit NRR. However, using the composite mechanism that includes the chemical NRR steps, different energetic spans are identified to limit Φ_{max} and thus the NRR activity (Figure 4B).

The activity predicted by the PCET mechanism increases linearly with more reducing biases, as shown in Figure 4A. Because every step of the PCET mechanism includes an electron transfer that becomes more favorable at more reducing biases, there is no limit to NRR activity predicted by the PCET mechanism. Consequently, the peak of the PCET volcano reaches Φ_{max} < 0 eV at a sufficiently reducing bias, indicating that all intermediate reaction steps are downhill. Furthermore, the PCET mechanism predicts a region of materials (shaded regions of Figure 4A) where the Φ_{max} for NRR is lower than the Φ_{max} for HER (see SI Section 2.5 for HER pathways and energies). These results for the PCET pathway suggest that optimal electrocatalyst materials that obey the identified scaling relations can provide high activity and selectivity toward NRR. However, this is not observed experimentally. 41 Instead, experimental observations have not identified any monometallic materials that provide high activity and selectivity toward NRR.^{7,41}

Conversely, the volcano plot for the composite mechanism is truncated by the chemical NH3* desorption step. As the applied potential becomes more reduced, the NH3* desorption line widens and truncates a larger width of the volcano. This leads to a nonlinear dependence of Φ_{max} on applied bias for materials that switch energetic spans at more reducing biases to the $NH_3^* \rightarrow NH_3$ chemical step (i.e., orange arrows in Figure 4B). The composite mechanism shows that materials at more reducing potentials are limited by the NH3* desorption step, which is less sensitive to the applied potential than PCET steps. However, by using GC-DFT to study the NH₂* chemical desorption step at each bias, we predict that the grand free energy for NH3* desorption is sensitive to the applied bias, resulting in a slight upward shift of the volcano's peak with more reducing potentials. This result would not be captured using a post hoc bias correction approach that does not include dipole and charging corrections.

For all studied materials, HER is calculated to have a lower $\Phi_{ ext{max}}$ (greater $-\Phi_{ ext{max}}$) than NRR using the composite mechanism (Figure 4B). Consequently, the results based on the composite mechanism suggest that all materials that obey the identified scaling relations for metals will have lower activity toward NRR than HER, based on their Φ_{max} . The direct calculation of NRR and HER activity was not performed here due to the significant additional computational expense required to perform transition state searches and microkinetic modeling for the three NRR pathways considered on the 30 studied surfaces. 16 The qualitative differences observed between the composite and PCET mechanisms highlight the importance of considering chemical, non-PCET steps in electrochemical reaction mechanisms and that these steps should be modeled at discrete biases using grand-canonical modeling approaches such as GC-DFT. Other chemisorbed NH₃* states (NNH₃*, NHNH₃*, and NH₂NH₃*) were also modeled to examine their impact on surface activity. These states are typically less stable than a coupled PCET and desorption of the first NH3 molecule, and including these states does not impact Φ_{max} for the studied surfaces (see SI

The predicted peak positions of the volcano plots are similar for both the PCET pathway and the composite mechanism at 0 V ($\Phi_{N^*,peak}$ = -0.61 and -0.73 eV, respectively), resulting in similar predictions of which materials lie near the peak of the volcano as well as a similar predicted ordering of materials based on NRR activity. The activity ordering of materials at 0 V therefore generally agrees with that of previous work.^{8,9} For example, both the PCET pathway and composite mechanism predict that Ru(111) is near the top of the NRR volcano due to its favorable scaling between intermediates, which agrees with previous modeling results on metals using PCET and CHE approaches.^{8,9} However, the consideration of multiple reaction pathways and the chemical NRR steps in the composite mechanism results in nonlinear changes in Φ_{max} on several surfaces as a function of applied bias. Consequently, the potential dependence of Φ_{max} observed for the composite mechanism deviates substantially from the simpler PCET mechanism and previous studies for some materials. This nonlinearity results in a large deviation of the peak positions between the PCET mechanism and composite mechanism at $-0.5 \text{ V } (\Phi_{\text{N*,peak}} = -0.94 \text{ and } -0.35 \text{ eV, respectively}), \text{ and a}$ greater potential dependence of Φ_{max} for some materials. This

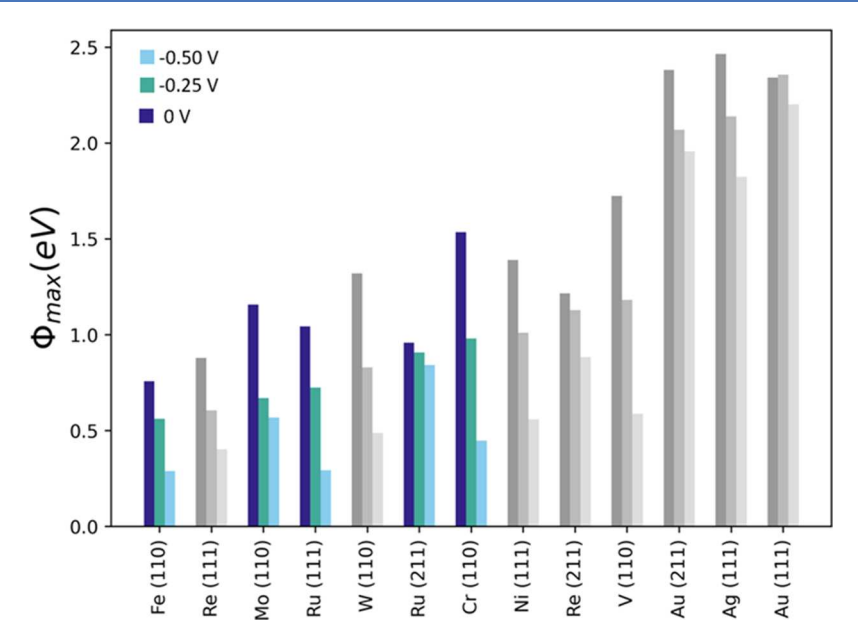


Figure 5. Bias dependence of Φ_{max} . A subset of the surfaces is shown to highlight the variation in how Φ_{max} changes with bias for the composite mechanism. Surfaces are sorted by the Φ_{max} value at -0.25 V. Materials of particular interest are shown in color.

results in different ordering of surfaces based on the NRR activity at different biases, as shown in Figure 5, which plots $\Phi_{\rm max}$ at each studied potential for a subset of surfaces using the composite mechanism.

Figure 5 illustrates the highly variable bias dependence of Φ_{max} for specific metal surfaces. For example, Mo(110) is an inactive catalyst at 0 V because of its large endergonic span $(\Phi_{\text{max}} = 1.16 \text{ eV})$ to protonate NH* twice to yield one NH₃ molecule. However, because two electron transfers are required to transform NH* into one NH₃ molecule, the energetic span on Mo(110) is highly sensitive to potential. This leads to a substantial decrease in Φ_{max} from 1.16 at 0 V to 0.67 eV at -0.25 V, making Mo(110) the third most active metal for catalyzing NRR at -0.25 V as predicted by Φ_{max} . However, by -0.5 V, Mo(110) becomes limited by the chemical step of NH₃* desorption and the energetic span of Mo(110) becomes minimally sensitive to bias ($\Phi_{\text{max}} = 0.57 \text{ eV}$ at -0.5 V). Consequently, the Φ_{max} for Mo(110) is predicted to shift nonlinearly with bias. In contrast, Ru(211) is minimally sensitive to changes in bias (Φ_{max} = 0.96 and 0.84 eV at 0.0 and -0.5 V, respectively) because its energetic span is always limited by the chemical step of NH₃* desorption. Consequently, Ru(211) is calculated to have the third lowest Φ_{max} of the studied surfaces at 0.0 V, but only the 16th lowest Φ_{max} at -0.5 V. The Φ_{max} of Ru(211) at -0.5 V deviates from previous studies that place it toward the top of the activity volcano, and suggests that Ru(111) is the more active facet of Ru at -0.5 V. The differences between Ru(111) and Ru(211) primarily arise from the different number of electron transfers associated with different energetic spans. However, the bias dependence of Φ_{max} on Ru(211) is a direct consequence of studying the chemical NRR steps with GC-DFT for each applied bias. We note that the Ru(0001) facet of HCP Ru and the Ru(111) facet of FCC Ru, which have an identical surface coordination environment, have comparable Φ_{N^*} and thus similar Φ_{max} (1.27 and 1.04 eV, respectively, at 0 V; see SI Section 2.2).

The materials that obey the identified scaling relations predicted in this study using Φ_{max} computed by GC-DFT are

limited by poor NRR activity and selectivity due to competition with HER. Thus, a commercially viable NRR process demands next-generation materials that break these scaling relations. In particular, superior NRR activity and selectivity may be achieved by materials with strong intermediate (i.e., N*) binding but disproportionately weak NH₃* binding, which lie in the upper left quadrant of Figure 4B. Weak NH₃* binding is necessary as this step may become $\Phi_{ ext{max}}$ limiting at more reducing potentials. Selective stabilization of early NRR intermediates or selective destabilization of NH₃* may enable this scaling-relation-breaking behavior. 16 The GC-DFT computed $\Delta\Phi$ values for adsorption of NH₃* and N* can provide initial screening criteria for a highthroughput approach to identify whether candidate materials deviate from the NH₃* desorption scaling line in Figure 3, which limits the highest activity metals. However, promising materials will need to be evaluated using additional intermediates (e.g., N_2H^* , NH^*) to identify their Φ_{max} and ultimately, using barriers calculated from transition states computed under electrochemical conditions to predict NRR kinetics. 16,43,44

CONCLUSIONS

This work demonstrates that the inclusion of both chemical and electrochemical steps, modeled here under explicit applied bias using GC-DFT, is necessary to capture the thermodynamic limitations for NRR on metals. Volcano plots derived from NRR scaling relations are truncated by the chemical NH₃* desorption step, which limits the energetic span, and Φ_{max} , on the highest activity surfaces and should be included in future studies to identify superior NRR electrocatalysts. Φ_{max} is observed to scale nonlinearly with bias on surfaces where the energetic span switches with the applied potential. The results presented herein are based on Φ_{max} , which provides a thermodynamic approximation of catalyst activity but neglects the explicit calculation of kinetic barriers. Thermodynamic screening descriptors are computationally inexpensive tools for sorting inactivate materials out of a large material space as well as understanding general activity trends within the space.

However, to quantitatively predict activity and selectivity for materials that lie near the top of the thermodynamic volcano, explicit transition state calculations coupled with microkinetic models are necessary. ^{16,43,44} Therefore, the validation of these results and the quantitative prediction of NRR activity and selectivity require follow-up investigations of NRR and HER kinetics that include transition-state calculations and microkinetic modeling.

While the current results are specific to the NRR on metals, these findings may have broader implications for studying other electrochemical reactions that include both chemical and electrochemical steps, such as CO2 reduction. The methodology applied in this work is broadly transferable and thus enables potential-dependent modeling of other electrochemical reactions and surfaces of more complex classes of materials (e.g., oxides, pnictides, chalcogenides, etc.). Thus, this approach is suitable for a high-throughput investigation to identify superior electrocatalysts for NRR that break the identified scaling relations. We are currently leveraging this approach to conduct a broader high-throughput investigation to study electrocatalysts for NRR and other key electrochemical reactions. The results from this subsequent effort, including energetics, structures, and calculated properties, will be published online in a planned database, which will provide a standardized platform to easily and efficiently analyze and compare electrocatalyst materials.

■ ASSOCIATED CONTENT

Data Availability Statement

Codes and data are available for free at https://github.com/cote3804/NRR data.

Supporting Information

The Supporting Information is available free of charge at https://pubs.acs.org/doi/10.1021/acscatal.3c01978.

Additional details of GC-DFT and Φ_{max} calculations, free energy diagrams, scaling relations, and data tables (PDF)

AUTHOR INFORMATION

Corresponding Authors

Nicholas R. Singstock — Department of Chemical and Biological Engineering, University of Colorado Boulder, Boulder, Colorado 80309, United States; Department of Mechanical Engineering, University of Colorado Boulder, Boulder, Colorado 80309, United States; orcid.org/0000-0003-2093-0216; Email: nicholas.singstock@colorado.edu

Charles B. Musgrave — Department of Chemical and Biological Engineering, University of Colorado Boulder, Boulder, Colorado 80309, United States; Materials Science and Engineering Program and Renewable and Sustainable Energy Institute, University of Colorado Boulder, Boulder, Colorado 80309, United States; orcid.org/0000-0002-5732-3180; Email: charles.musgrave@colorado.edu

Authors

Cooper R. Tezak – Department of Chemical and Biological Engineering, University of Colorado Boulder, Boulder, Colorado 80309, United States

Abdulaziz W. Alherz — Department of Chemical Engineering, College of Engineering and Petroleum, Kuwait University, Safat 13060, Kuwait; oorcid.org/0000-0001-7529-3483

Derek Vigil-Fowler – National Renewable Energy Laboratory, Arvada, Colorado 80007, United States

Christopher A. Sutton — Department of Chemistry and Biochemistry, University of South Carolina, Columbia, South Carolina 29208, United States; ⊙ orcid.org/0000-0003-1206-8080

Ravishankar Sundararaman — Materials Science and Engineering, Rensselaer Polytechnic Institute, Troy, New York 12180, United States; orcid.org/0000-0002-0625-4592

Complete contact information is available at: https://pubs.acs.org/10.1021/acscatal.3c01978

Author Contributions

◆C.R.T. and N.R.S. contributed equally. All authors contributed to the development of the calculation methodology and the standardized calculation parameters. C.R.T. and N.R.S. ran the calculations. N.R.S. developed scripts to run high-throughput calculations. C.R.T. analyzed the data, created the figures, and drafted the manuscript. C.R.T., N.R.S., and C.B.M. conceived the project. All authors reviewed and edited the manuscript.

Notes

The authors declare no competing financial interest.

ACKNOWLEDGMENTS

All authors acknowledge support from the U.S. Department of Energy, Office of Science, Basic Energy Sciences (DE-SC0022247). N.R.S. and C.B.M. also acknowledge support from the National Science Foundation (CBET-2016225). This research used resources of the National Energy Research Scientific Computing Center, a DOE Office of Science User Facility supported by the Office of Science of the U.S. Department of Energy under Contract No. DE-AC02-05CH11231 using NERSC award BES-ERCAP0024200. A portion of the research was performed using computational resources sponsored by the Department of Energy's Office of Energy Efficiency and Renewable Energy and located at the National Renewable Energy Laboratory. A portion of this work utilized the Alpine high performance computing resource at the University of Colorado Boulder. Alpine is jointly funded by the University of Colorado Boulder, the University of Colorado Anschutz, and Colorado State University..

ABBREVIATIONS

NRR, nitrogen reduction reaction; HER, hydrogen evolution reaction; GC-DFT, grand-canonical density functional theory; PCET, proton-coupled electron transfer; SHE, standard hydrogen electrode; CHE, computational hydrogen electrode method

REFERENCES

- (1) Sandalow, D.; Aines, R.; Fan, Z.; Friedmann, A.; McCormick, C.; Merz, A.-K.; Scown, C.Innovation for Cool Earth Forum. In *Low-Carbon Ammonia Roadmap*; Innovation for Cool Earth Forum (ICEF), 2022.
- (2) Barker, D.; Brown, T.; Cook, N. Green Ammonia; Royal Society,
- (3) Smith, C.; Hill, A.; Torrente-Murciano, L. Current and Future Role of Haber–Bosch Ammonia in a Carbon-Free Energy Landscape. *Energy Environ. Sci.* **2020**, *13* (2), 331–344.
- (4) Muhich, C. L.; Ehrhart, B. D.; Al-Shankiti, I.; Ward, B. J.; Musgrave, C. B.; Weimer, A. W. A Review and Perspective of Efficient

- Hydrogen Generation via Solar Thermal Water Splitting. WIREs Energy Environ. 2016, 5 (3), 261–287.
- (5) Hochman, G.; Goldman, A. S.; Felder, F. A.; Mayer, J. M.; Miller, A. J. M.; Holland, P. L.; Goldman, L. A.; Manocha, P.; Song, Z.; Aleti, S. Potential Economic Feasibility of Direct Electrochemical Nitrogen Reduction as a Route to Ammonia. *ACS Sustainable Chem. Eng.* **2020**, *8* (24), 8938–8948.
- (6) Martín, A. J.; Pérez-Ramírez, J. Heading to Distributed Electrocatalytic Conversion of Small Abundant Molecules into Fuels, Chemicals, and Fertilizers. *Joule* **2019**, 3 (11), 2602–2621.
- (7) Chanda, D.; Xing, R.; Xu, T.; Liu, Q.; Luo, Y.; Liu, S.; Tufa, R. A.; Dolla, T. H.; Montini, T.; Sun, X. Electrochemical Nitrogen Reduction: Recent Progress and Prospects. *Chem. Commun.* **2021**, *57* (60), 7335–7349.
- (8) Montoya, J. H.; Tsai, C.; Vojvodic, A.; Nørskov, J. K. The Challenge of Electrochemical Ammonia Synthesis: A New Perspective on the Role of Nitrogen Scaling Relations. *ChemSusChem* **2015**, 8 (13), 2180–2186.
- (9) Skúlason, E.; Bligaard, T.; Gudmundsdóttir, S.; Studt, F.; Rossmeisl, J.; Abild-Pedersen, F.; Vegge, T.; Jónsson, H.; K Nørskov, J. A Theoretical Evaluation of Possible Transition Metal Electro-Catalysts for N 2 Reduction. *Phys. Chem. Chem. Phys.* **2012**, *14* (3), 1235–1245.
- (10) Ying, Y.; Fan, K.; Qiao, J.; Huang, H. Rational Design of Atomic Site Catalysts for Electrocatalytic Nitrogen Reduction Reaction: One Step Closer to Optimum Activity and Selectivity. *Electrochem. Energy Rev.* **2022**, 5 (3), 6.
- (11) Höskuldsson, Á. B.; Tayyebi, E.; Skúlason, E. Computational Examination of the Kinetics of Electrochemical Nitrogen Reduction and Hydrogen Evolution on a Tungsten Electrode. *J. Catal.* **2021**, 404, 362–370.
- (12) Yeo, B. C.; Kong, J.; Kim, D.; Goddard, W. A. I.; Park, H. S.; Han, S. S. Electronic Structural Origin of the Catalytic Activity Trend of Transition Metals for Electrochemical Nitrogen Reduction. *J. Phys. Chem. C* 2019, 123 (51), 31026–31031.
- (13) Abghoui, Y.; Garden, A. L.; Howalt, J. G.; Vegge, T.; Skúlason, E. Electroreduction of N2 to Ammonia at Ambient Conditions on Mononitrides of Zr, Nb, Cr, and V: A DFT Guide for Experiments. ACS Catal. 2016, 6 (2), 635–646.
- (14) Abghoui, Y.; Garden, A. L.; Hlynsson, V. F.; Björgvinsdóttir, S.; Ólafsdóttir, H.; Skúlason, E. Enabling Electrochemical Reduction of Nitrogen to Ammonia at Ambient Conditions through Rational Catalyst Design. *Phys. Chem. Chem. Phys.* **2015**, *17* (7), 4909–4918.
- (15) Ling, C.; Ouyang, Y.; Li, Q.; Bai, X.; Mao, X.; Du, A.; Wang, J. A General Two-Step Strategy—Based High-Throughput Screening of Single Atom Catalysts for Nitrogen Fixation. *Small Methods* **2019**, 3 (9), No. 1800376.
- (16) Singstock, N. R.; Musgrave, C. B. How the Bioinspired Fe2Mo6S8 Chevrel Breaks Electrocatalytic Nitrogen Reduction Scaling Relations. *J. Am. Chem. Soc.* **2022**, *144* (28), 12800–12806.
- (17) Liu, X.; Jiao, Y.; Zheng, Y.; Jaroniec, M.; Qiao, S.-Z. Building Up a Picture of the Electrocatalytic Nitrogen Reduction Activity of Transition Metal Single-Atom Catalysts. *J. Am. Chem. Soc.* **2019**, *141* (24), 9664–9672.
- (18) Sundararaman, R.; Letchworth-Weaver, K.; Schwarz, K. A.; Gunceler, D.; Ozhabes, Y.; Arias, T. A. JDFTx: Software for Joint Density-Functional Theory. *SoftwareX* **2017**, *6*, 278–284.
- (19) Sundararaman, R.; Goddard, W. A. The Charge-Asymmetric Nonlocally Determined Local-Electric (CANDLE) Solvation Model. *J. Chem. Phys.* **2015**, *142* (6), No. 064107.
- (20) Brimley, P.; Almajed, H.; Alsunni, Y.; Alherz, A. W.; Bare, Z. J. L.; Smith, W. A.; Musgrave, C. B. Electrochemical CO2 Reduction over Metal-/Nitrogen-Doped Graphene Single-Atom Catalysts Modeled Using the Grand-Canonical Density Functional Theory. *ACS Catal.* **2022**, *12* (16), 10161–10171.
- (21) Kozuch, S.; Shaik, S. Kinetic-Quantum Chemical Model for Catalytic Cycles: The Haber-Bosch Process and the Effect of Reagent Concentration. *J. Phys. Chem. A* **2008**, *112* (26), 6032–6041.

- (22) Kozuch, S.; Shaik, S. How to Conceptualize Catalytic Cycles? The Energetic Span Model. Acc. Chem. Res. 2011, 44 (2), 101–110.
- (23) Razzaq, S.; Exner, K. S. Materials Screening by the Descriptor $Gmax(\eta)$: The Free-Energy Span Model in Electrocatalysis. *ACS Catal.* **2023**, 13 (3), 1740–1758.
- (24) Exner, K. S. A Universal Descriptor for the Screening of Electrode Materials for Multiple-Electron Processes: Beyond the Thermodynamic Overpotential. *ACS Catal.* **2020**, *10* (21), 12607–12617.
- (25) Kozuch, S. A Refinement of Everyday Thinking: The Energetic Span Model for Kinetic Assessment of Catalytic Cycles. *WIREs Comput. Mol. Sci.* **2012**, 2 (5), 795–815.
- (26) Kozuch, S.; Shaik, S. A Combined Kinetic-Quantum Mechanical Model for Assessment of Catalytic Cycles: Application to Cross-Coupling and Heck Reactions. *J. Am. Chem. Soc.* **2006**, *128* (10), 3355–3365.
- (27) Exner, K. S.; Sohrabnejad-Eskan, I.; Over, H. A Universal Approach To Determine the Free Energy Diagram of an Electrocatalytic Reaction. *ACS Catal.* **2018**, *8* (3), 1864–1879.
- (28) Cohen, M.; Vlachos, D. G. Modified Energy Span Analysis of Catalytic Parallel Pathways and Selectivity. *Ind. Eng. Chem. Res.* **2023**, 62 (5), 2191–2201.
- (29) Kozuch, S. Steady State Kinetics of Any Catalytic Network: Graph Theory, the Energy Span Model, the Analogy between Catalysis and Electrical Circuits, and the Meaning of "Mechanism. ACS Catal. 2015, 5 (9), 5242–5255.
- (30) Xia, Z.; Xiao, H. Grand Canonical Ensemble Modeling of Electrochemical Interfaces Made Simple. *J. Chem. Theory Comput.* **2023**, *19*, 5168.
- (31) Kastlunger, G.; Lindgren, P.; Peterson, A. A. Controlled-Potential Simulation of Elementary Electrochemical Reactions: Proton Discharge on Metal Surfaces. *J. Phys. Chem. C* **2018**, *122* (24), 12771–12781.
- (32) Song, J.; Kwon, S.; Hossain, M. D.; Chen, S.; Li, Z.; Goddard, W. A. Reaction Mechanism and Strategy for Optimizing the Hydrogen Evolution Reaction on Single-Layer 1T' WSe2 and WTe2 Based on Grand Canonical Potential Kinetics. ACS Appl. Mater. Interfaces 2021, 13 (46), 55611–55620.
- (33) Jain, A.; Ong, S. P.; Hautier, G.; Chen, W.; Richards, W. D.; Dacek, S.; Cholia, S.; Gunter, D.; Skinner, D.; Ceder, G.; Persson, K. A. Commentary: The Materials Project: A Materials Genome Approach to Accelerating Materials Innovation. *APL Mater.* **2013**, *1* (1), No. 011002.
- (34) Tran, R.; Xu, Z.; Radhakrishnan, B.; Winston, D.; Sun, W.; Persson, K. A.; Ong, S. P. Surface Energies of Elemental Crystals. *Sci. Data* **2016**, 3 (1), No. 160080.
- (35) Larsen, A. H.; Mortensen, J. J.; Blomqvist, J.; Castelli, I. E.; Christensen, R.; Dułak, M.; Friis, J.; Groves, M. N.; Hammer, B.; Hargus, C.; Hermes, E. D.; Jennings, P. C.; Jensen, P. B.; Kermode, J.; Kitchin, J. R.; Kolsbjerg, E. L.; Kubal, J.; Kaasbjerg, K.; Lysgaard, S.; Maronsson, J. B.; Maxson, T.; Olsen, T.; Pastewka, L.; Peterson, A.; Rostgaard, C.; Schiøtz, J.; Schütt, O.; Strange, M.; Thygesen, K. S.; Vegge, T.; Vilhelmsen, L.; Walter, M.; Zeng, Z.; Jacobsen, K. W. The Atomic Simulation Environment—a Python Library for Working with Atoms. J. Phys.: Condens. Matter 2017, 29 (27), No. 273002.
- (36) Perdew, J. P.; Burke, K.; Ernzerhof, M. Generalized Gradient Approximation Made Simple. *Phys. Rev. Lett.* **1996**, 77 (18), 3865–3868.
- (37) Grimme, S.; Antony, J.; Ehrlich, S.; Krieg, H. A Consistent and Accurate Ab Initio Parametrization of Density Functional Dispersion Correction (DFT-D) for the 94 Elements H-Pu. *J. Chem. Phys.* **2010**, 132 (15), No. 154104.
- (38) Gunceler, D.; Letchworth-Weaver, K.; Sundararaman, R.; Schwarz, K. A.; Arias, T. A. The Importance of Nonlinear Fluid Response in Joint Density-Functional Theory Studies of Battery Systems. *Modell. Simul. Mater. Sci. Eng.* **2013**, *21* (7), No. 074005.
- (39) Burgess, D. NIST Chemistry WebBook, NIST Standard Reference Database Number 69; Linstrom, P. J.; Mallard, W. G., Eds.; National Institute of Standards and Technology: Gaithersburg, MD, 2011.

- (40) Howalt, J. G.; Bligaard, T.; Rossmeisl, J.; Vegge, T. DFT Based Study of Transition Metal Nano-Clusters for Electrochemical NH 3 Production. *Phys. Chem. Chem. Phys.* **2013**, 15 (20), 7785–7795.
- (41) Andersen, S. Z.; Čolić, V.; Yang, S.; Schwalbe, J. A.; Nielander, A. C.; McEnaney, J. M.; Enemark-Rasmussen, K.; Baker, J. G.; Singh, A. R.; Rohr, B. A.; Statt, M. J.; Blair, S. J.; Mezzavilla, S.; Kibsgaard, J.; Vesborg, P. C. K.; Cargnello, M.; Bent, S. F.; Jaramillo, T. F.; Stephens, I. E. L.; Nørskov, J. K.; Chorkendorff, I. A Rigorous Electrochemical Ammonia Synthesis Protocol with Quantitative Isotope Measurements. *Nature* 2019, 570 (7762), 504–508.
- (42) Domínguez-Flores, F.; Melander, M. M. Approximating Constant Potential DFT with Canonical DFT and Electrostatic Corrections. J. Chem. Phys. 2023, 158 (14), No. 144701.
- (43) Lindgren, P.; Kastlunger, G.; Peterson, A. A. A Challenge to the $G \sim 0$ Interpretation of Hydrogen Evolution. *ACS Catal.* **2020**, *10* (1), 121–128.
- (44) Adams, J. S.; Chemburkar, A.; Priyadarshini, P.; Ricciardulli, T.; Lu, Y.; Maliekkal, V.; Sampath, A.; Winikoff, S.; Karim, A. M.; Neurock, M.; Flaherty, D. W. Solvent Molecules Form Surface Redox Mediators in Situ and Cocatalyze O2 Reduction on Pd. *Science* **2021**, 371 (6529), 626–632.

☐ Recommended by ACS

Symmetry-Breaking p-Block Antimony Single Atoms Trigger N-Bridged Titanium Sites for Electrocatalytic Nitrogen Reduction with High Efficiency

Hongfei Gu, Wenxing Chen, et al.

NOVEMBER 01, 2023

ACS NANO

READ 🗹

Rapid Aqueous Ammonia Oxidation to N_2 Using a Molecular Ru Electrocatalyst

Samuel I. Jacob, Gabriel Ménard, et al.

AUGUST 14, 2023

ACS ENERGY LETTERS

READ 🗹

DFT-kMC Analysis for Identifying Novel Bimetallic Electrocatalysts for Enhanced NRR Performance by Suppressing HER at Ambient Conditions Via Active-Site ...

Chi Ho Lee, Joseph Sang-Il Kwon, et al.

DECEMBER 06, 2022

ACS CATALYSIS

READ 🗹

Hydrogen Radical-Induced Electrocatalytic N_2 Reduction at a Low Potential

Xueting Feng, Jin Zhang, et al.

APRIL 25, 2023

JOURNAL OF THE AMERICAN CHEMICAL SOCIETY

READ 🗹

Get More Suggestions >